

Decoupling Minimal Surface Metamaterial Properties Through Multi-Material Hyperbolic Tilings

Callens, Sebastien J.P.; Arns, Christoph H.; Kuliesh, Alina; Zadpoor, Amir A.

DOI

[10.1002/adfm.202101373](https://doi.org/10.1002/adfm.202101373)

Publication date

2021

Document Version

Final published version

Published in

Advanced Functional Materials

Citation (APA)

Callens, S. J. P., Arns, C. H., Kuliesh, A., & Zadpoor, A. A. (2021). Decoupling Minimal Surface Metamaterial Properties Through Multi-Material Hyperbolic Tilings. *Advanced Functional Materials*, 31(30), Article 2101373. <https://doi.org/10.1002/adfm.202101373>

Important note

To cite this publication, please use the final published version (if applicable). Please check the document version above.

Copyright

Other than for strictly personal use, it is not permitted to download, forward or distribute the text or part of it, without the consent of the author(s) and/or copyright holder(s), unless the work is under an open content license such as Creative Commons.

Takedown policy

Please contact us and provide details if you believe this document breaches copyrights. We will remove access to the work immediately and investigate your claim.

Decoupling Minimal Surface Metamaterial Properties Through Multi-Material Hyperbolic Tilings

Sebastien J. P. Callens,* Christoph H. Arns, Alina Kuliessh, and Amir A. Zadpoor

Rapid advances in additive manufacturing have kindled widespread interest in the rational design of metamaterials with unique properties over the past decade. However, many applications require multi-physics metamaterials, where multiple properties are simultaneously optimized. This is challenging since different properties, such as mechanical and mass transport properties, typically impose competing requirements on the nano-/micro-/meso-architecture of metamaterials. Here, a parametric metamaterial design strategy that enables independent tuning of the effective permeability and elastic properties is proposed. Hyperbolic tiling theory is applied to devise simple templates, based on which triply periodic minimal surfaces (TPMS) are partitioned into hard and soft regions. Through computational analyses, it is demonstrated how the decoration of hard, soft, and void phases within the TPMS substantially enhances their permeability–elasticity property space and offers high tunability in the elastic properties and anisotropy at constant permeability. Also shown is that this permeability–elasticity balance is well captured using simple scaling laws. The proposed concept is demonstrated through multi-material additive manufacturing of representative specimens. The approach, which is generalizable to other designs, offers a route towards multi-physics metamaterials that need to simultaneously carry a load and enable mass transport, such as load-bearing heat exchangers or architected tissue-substituting meta-biomaterials.

connection has been leveraged to develop metamaterials with unique, unusual, and extreme acoustic,^[1] photonic,^[2] or mechanical properties.^[3] Historically, most types of metamaterial architectures have been based on periodic arrangements of struts, often inspired by crystallographic lattices.^[4] In search for higher mass-specific mechanical properties, periodic plate-lattices have been proposed, capable of storing strain energy more efficiently.^[5] More recently, smooth shell-based lattices have also attracted great interest, since these architectures are devoid of the stress concentrations that are inherent at the intersections of strut- or plate-lattices, and since their intrinsically curved morphology endows them with high specific stiffness and attractive energy absorption behavior.^[6] Among the shell-based metamaterials, those derived from triply periodic minimal surfaces (TPMS) have most widely been studied.^[7] These are bicontinuous, infinitely-extending, saddle-shaped surfaces that locally minimize area and have the defining characteristic of zero mean curvature ($H = 0$) at every

1. Introduction


The fundamental paradigm of metamaterials is that their macroscale properties are largely driven by their nano-, micro-, or mesoscale architecture. This intimate structure-property

point along the surface.^[8] The widespread interest in TPMS-based structures has partly been fueled by their intriguing mathematical foundation and their widespread observations in spontaneously-assembled natural systems,^[9] but is also due to their attractive and extremal physical properties.^[10]

Irrespective of the architecture type, the central challenge in metamaterial design is to optimize the material geometry to attain the desired macroscale physical properties. In the case of multi-physics metamaterials, however, several properties are targeted simultaneously. It turns out that optimizing the geometry for one property often leads to a decrease in the performance with respect to the others. This is exemplified in architected tissue scaffolds, or “meta-biomaterials”,^[11] where the material geometry has conflicting effects on the mechanical and mass transport functionality:^[12] increasing the mechanical properties, by increasing the relative density of the metamaterial,^[13] generally results in a decreased fluid permeability. A notable example where the decoupling of these properties is somewhat possible is a pentamode metamaterial, consisting of spindle-shaped struts that meet at relatively weak nodes.^[14] The mechanical properties of these materials mainly depend on the node geometry and not on the overall relative density, offering the ability to partially tune the permeability independently of the mechanical

S. J. P. Callens, A. Kuliessh, Prof. A. A. Zadpoor
Department of Biomechanical Engineering
TU Delft
Mekelweg 2, Delft 2628CD, The Netherlands
E-mail: s.j.p.callens@tudelft.nl

Prof. C. H. Arns
School of Minerals and Energy Resources Engineering
The University of New South Wales
Sydney, New South Wales 2052, Australia

 The ORCID identification number(s) for the author(s) of this article can be found under <https://doi.org/10.1002/adfm.202101373>.

© 2021 The Authors. Advanced Functional Materials published by Wiley-VCH GmbH. This is an open access article under the terms of the Creative Commons Attribution-NonCommercial License, which permits use, distribution and reproduction in any medium, provided the original work is properly cited and is not used for commercial purposes.

DOI: 10.1002/adfm.202101373

properties.^[15] However, this ability is limited, because the upper bound on permeability is constrained by the desired mechanical properties, and because pentamode metamaterials inherently rely on highly-specific strut-based architectures. As an alternative, one could consider scaling of the unit cells. A uniform scaling of the unit cell length by a factor l does not affect the elastic properties of the lattice, while the absolute permeability scales with l^2 . This implies that one could tune both properties somewhat independently, merely by scaling the structure.^[12c] However, in many applications of multifunctional metamaterials, the unit cell size is not a parameter that could freely be altered, at least not without affecting other relevant properties or violating the requirements of the applied manufacturing processes. In meta-biomaterials, for example, the pore size should remain within experimentally determined bounds to promote tissue regeneration.^[16] Moreover, scaling of the unit cell size would also affect properties, such as overall cell attachment or biodegradation behavior, which are dependent on the specific surface area and scale with l^{-1} .^[12c] Furthermore, the resolution of the additive manufacturing process or the desired number of unit cells to obtain sufficiently homogenized behavior could impose additional constraints on unit cell scaling.

An attractive and more potent strategy to unlock a larger metamaterial design space is to spatially distribute multiple materials with widely different properties, instead of architecting only a single material. This approach has only recently become possible, owing to advances in multi-material additive manufacturing, and has enabled the design of mechanical metamaterials and composites with exotic deformation modes and tunable Poisson's ratios.^[17] Here, we leverage the multi-material strategy to develop periodic metamaterials with independently tunable properties. While the multi-material paradigm could be applied to a wide range of metamaterial designs, we propose a strategy to parametrically develop biphasic, TPMS-based architectures that interpolate between strut- and shell-lattices. Our focus on TPMS structures originates from the recent and widespread interest in these metamaterial designs for structural and biomedical applications, as well as their attractive combinations of mechanical and transport properties, which has often led to them being classified as multifunctional metamaterials.^[7a,12c,d,18] Additionally, our strategy directly builds upon the geometrical definition and the inherent hyperbolic symmetries of TPMS, offering a robust and straightforward approach to tailor unit cell geometry and the spatial distribution of the different materials. This enables us to decouple the mechanical and mass transport properties to an extent that is not possible in uniphase metamaterials. Using computational homogenization, we determine the effective elastic properties and anisotropy of a wide range of structures as a function of the unit cell geometry and material choice. Moreover, we quantify the intrinsic permeability (i.e., normalized by unit cell length) of the metamaterials using computational fluid dynamics (CFD). Our results confirm that our parametric design strategy and the combination of two different materials significantly expands the achievable space of multi-physics properties and greatly enhances the ability to independently tune the permeability and elastic properties. Additionally, we demonstrate the proposed concept by additively manufacturing and mechanically testing metamaterials that combine hard and

soft polymers. While we focus here on two types of TPMS, this concept is directly extendable to other types of TPMS and could also be generalized to other types of shell-lattices, even those of a stochastic nature.

2. Results

2.1. Triply Periodic Networks from Hyperbolic Tilings

The foundation of our design approach is the intimate connection between TPMS and the hyperbolic geometry: the geometry of saddle shapes (with negative Gaussian curvature). Every TPMS can be constructed from a single, fundamental patch that is symmetrically patterned throughout 3D space. This repeating pattern corresponds to a triangular tiling on the hyperbolic plane \mathbb{H}^2 . Essentially, this implies that a portion of 2D hyperbolic space (\mathbb{H}^2) can be projected onto a TPMS (with minor distortions) in 3D Euclidean space (\mathbb{E}^3), in a manner similar to how a portion of the 2D Euclidean plane (\mathbb{E}^2) can be embedded in \mathbb{E}^3 by wrapping it on a cylinder.^[19] Here, we focus on two well-known TPMS of cubic symmetry, namely the P (primitive) and G (gyroid) surfaces. Both of these surfaces belong to the same TPMS family—they are related through the so-called Bonnet transformation—and they can both be derived from the same hyperbolic tiling. This hyperbolic tiling is called the *246 tiling (using orbifold notation), and consists of a repeating triangular patch with angles $\pi/2$, $\pi/4$, and $\pi/6$ (Figure 1a).

The remarkable connection between the hyperbolic plane and the TPMS enables the creation of a vast set of convoluted 3D networks, six of which are used as a template in this study. By decorating \mathbb{H}^2 with a periodic line pattern, that is, a tiling that is a subgroup of the *246 tiling, and by wrapping that line pattern onto the P or G minimal surface, a periodic 3D network, or surface reticulation, is obtained.^[19,20] Here, we consider three different hyperbolic tilings that give rise to six periodic networks, though many other tilings are available to generate different networks^[20c] (Figure 1b–d). The three hyperbolic tilings are obtained by drawing lines along one of the three edges of the fundamental patch. For example, the “26” tiling (Figure 1b) is obtained by connecting the edges between the $\pi/2$ and $\pi/6$ angles of all triangular patches. All of the six surface reticulations that we design are topologically equivalent to 3D networks that are known in reticular chemistry.^[21] For example, the P_{24} and G_{46} surface reticulations correspond to the crystal network structures of the minerals sodalite and garnet, respectively. Notably, the same hyperbolic tiling wrapped onto the P or G surface results in substantially different networks from a topological perspective. For example, the “26” tiling (Figure 1b) on the P surface generates a network with a primitive cubic topology of genus 3 (per unit cell), while the same tiling on the G surface generates a much more complex network with genus 17, even though the P and G surfaces themselves are both of genus 3. It is interesting to note that the P_{46} network consists entirely out of (Euclidean) straight lines, which is not the case for the other networks (Figure 1d). In fact, only a specific subset of TPMS, the so-called spanning minimal surfaces,^[22] have embedded straight lines, a property that is not shared by the G surface.

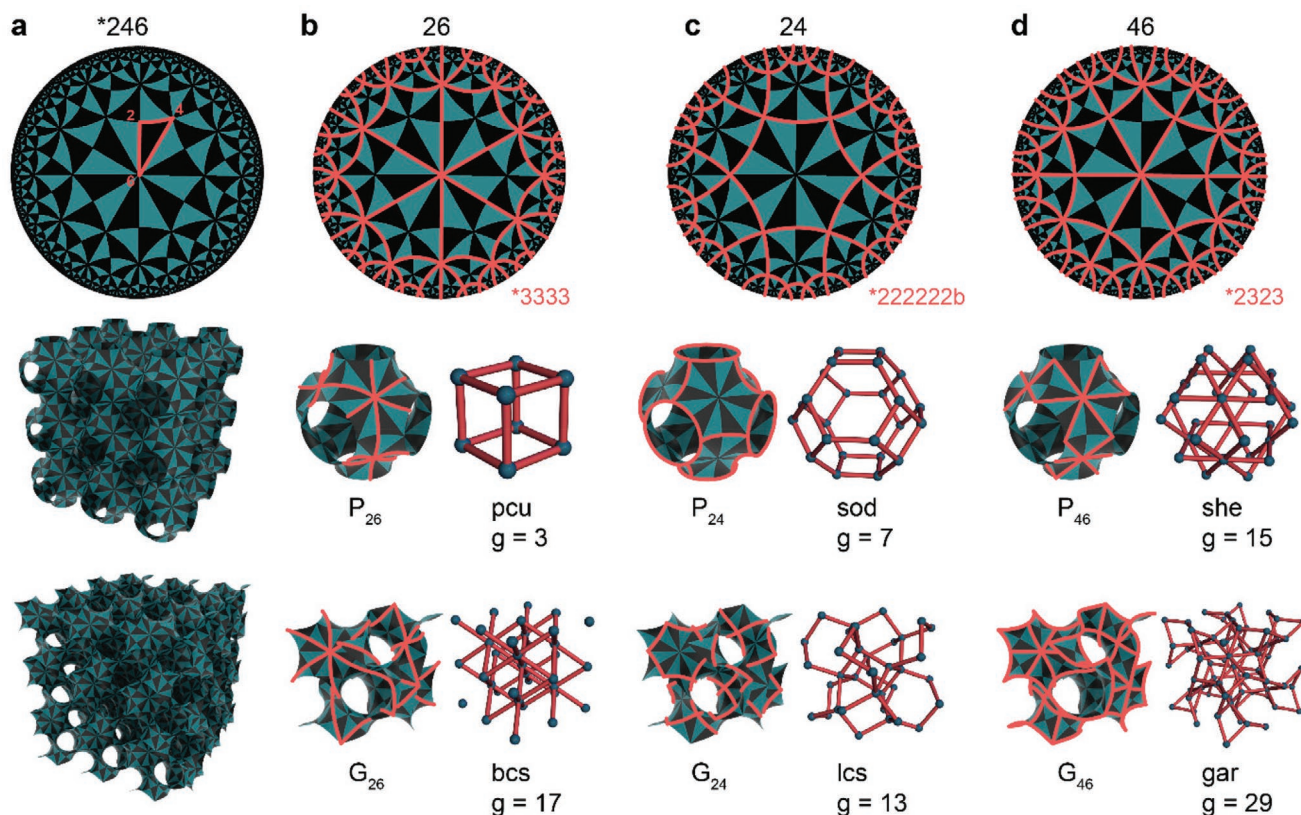


Figure 1. Hyperbolic tilings projected onto TPMS. a) The $*246$ hyperbolic tiling shown in the Poincaré disk model, with the fundamental triangular patch highlighted in red (top). The same hyperbolic tiling projected onto 27 translational unit cells of the P (middle) and G (bottom) surfaces. b) The “26” tiling in the Poincaré disk model (top) that results in two distinct networks on the P (middle) and G (bottom) surfaces. The orbifold naming of the tiling is indicated with red digits ($*3333$) and the RCSR naming^[21] of the 3D net topology is indicated with three letters (pcu and bcs). We show both the network by its embedding in the TPMS (left) as well as its canonical form (right),^[20c] which are topologically equivalent. The genus of the network (per unit cell) is indicated by g . c,d) Analogous to (b), but now for the “24” and “46” hyperbolic tilings.

2.2. Parametric Design of Biphasic Strut-Shell Metamaterials

The realization of 3D networks embedded in the P and G surfaces is the starting point of our strategy to parametrically design biphasic metamaterials. Essentially, our approach consists of “widening” these embedded networks to a desired degree, in order to form skeleton-like decorations on the TPMS that are templates to rationally distribute hard and soft phases (Figure 2). To construct the decorated translational unit cells of the P and G surfaces, we used the formal Enneper–Weierstrass parametrization.^[23] This parametrization maps an integration domain in the complex plane \mathbb{C}^2 to the fundamental patch in \mathbb{E}^3 , which is then symmetrically patterned to form the translational unit cell (Experimental Section). The simplicity of the integration domain enabled us to easily label portions of it with either a hard or a soft phase. This labeling is transferred to the unit cell through the Enneper–Weierstrass mapping. Thus, all the information required to rationally design a multi-material lattice consisting of an arbitrary number of unit cells is contained within the hard/soft-labeling of the fundamental patch and the inherent TPMS symmetry operations. We based the labeling of the integration domain on the previously described hyperbolic tilings: the domain is subdivided into different regions through lines that are parallel to one of the three domain edges (Figure 2a). This subdivision is parametrized by two offset parameters $\varphi_h \in [0, 1]$

and $\varphi_s \in [0, 1]$, which respectively control the amount of hard and soft phases and are defined such that $\varphi_h + \varphi_s \leq 1$. This parametrization is continuous, in the sense that φ_h and φ_s need not be selected from a discrete set of values, but can take any value within the admissible range. The default scenario is to set $\varphi_s = 1 - \varphi_h$ and vary the offset parameter of the hard phase. When $\varphi_h = 0$ or $\varphi_h = 1$, the unit cell entirely consists of a soft or a hard phase, respectively. Any intermediate value of φ_h results in a biphasic partitioning of the unit cell, whereby the hard phase interpolates between predominantly strut-like or shell-like architectures (Figure 2a). It is also possible to decrease the offset parameter of the soft phase such that $\varphi_h + \varphi_s < 1$. In this case, not all points in the integration domain are utilized in the Enneper–Weierstrass mapping, and an incomplete fundamental patch is obtained. This results in a unit cell with additional openings as opposed to the traditional P or G morphology (Figure 2b).

We converted the zero-thickness surfaces into solid metamaterial unit cells by bidirectionally thickening the surface in the normal direction by a fraction of the bounding box width (Figure 2a,b). Using the three hyperbolic tilings shown in Figure 1, six distinct biphasic metamaterial morphologies could be generated with tunable amounts of hard and soft materials (by varying φ_s and φ_h). We termed the designs with $\varphi_s + \varphi_h = 1$ “full” structures, and the designs with $\varphi_s + \varphi_h < 1$ “skeleton” structures (Figure 2b). The full biphasic designs with $\varphi_s = 1 - \varphi_h$

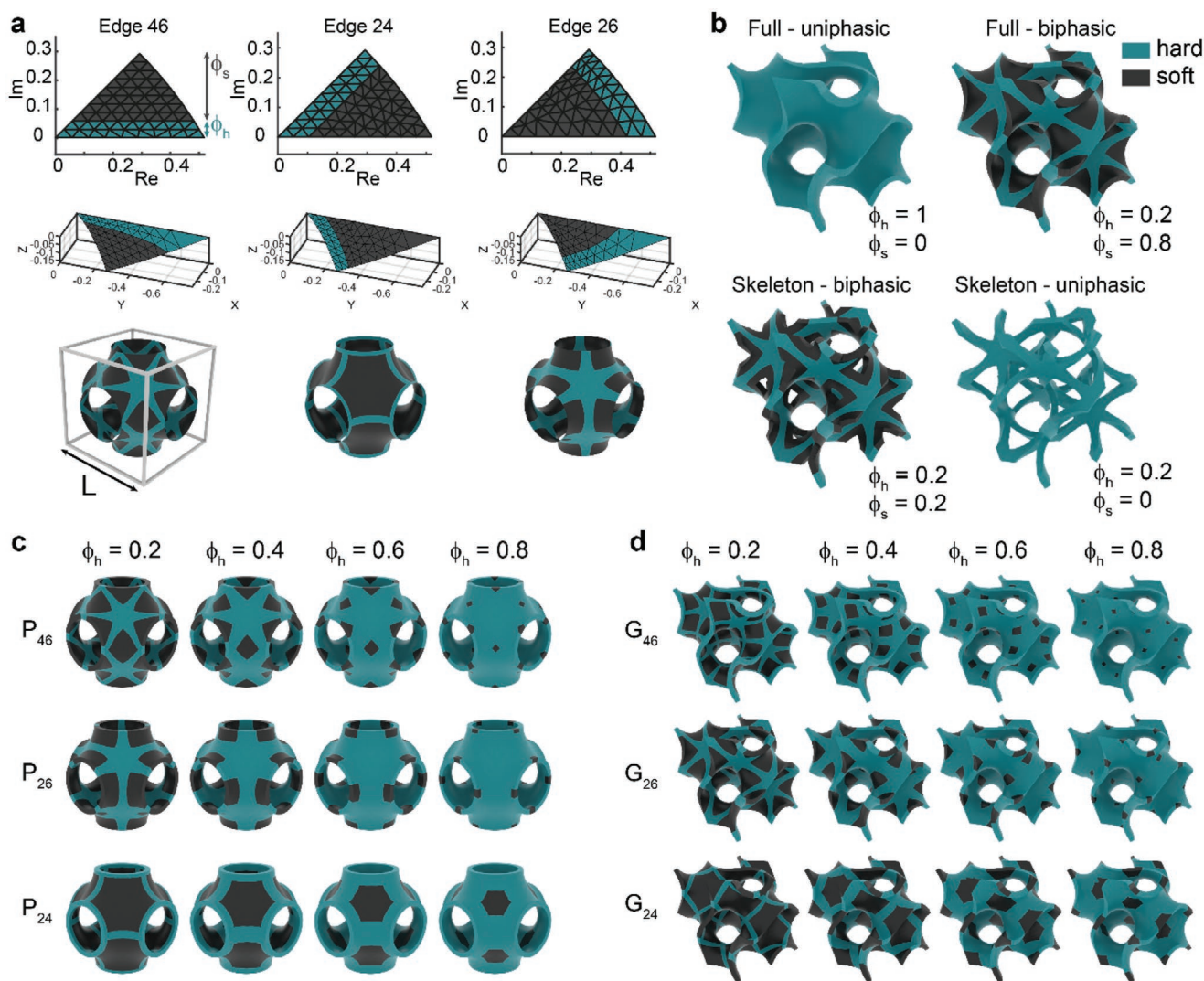


Figure 2. Parametric design approach for biphasic TPMS. a) Top row: the integration domain in the complex plane \mathbb{C}^2 that is parametrically partitioned into hard and soft regions for the “46,” “24,” and “26” designs. Middle row: the integration domain is mapped to \mathbb{E}^3 through the Enneper–Weierstrass parametrization, resulting in saddle-shaped fundamental patch with a biphasic partition. Bottom row: the cubic translational unit cell of the P surface obtained through symmetry operations on the fundamental patches of the middle row, with L indicating the cubic bounding box width (left most unit cell). b) The different types of uni- and biphasic unit cell designs derived from the G surface. c, d) Metamaterial unit cells for the three P and G designs, respectively. In all cases, $\phi_s + \phi_h = 1$ and ϕ_h is varied between 0.2 and 0.8.

shown in Figure 2c,d all have the same overall morphology, that is, that of the standard P or G surface, yet exhibit widely different material decorations. It is important to observe that the hard phase always forms a triply connected structure, while the soft phase consists of isolated inclusions. For sufficiently small values of ϕ_h , the hard phase essentially forms a strut-like skeleton that reinforces the predominantly soft-phased unit cell. For the larger values of ϕ_h , the area of the soft inclusions diminishes and the hard-phased skeleton approaches the shell-like morphology of the original unit cell.

2.3. Morphology of Biphasic TPMS-Based Metamaterials

The defining characteristic of TPMS is their specific curvature profile: they are defined as surfaces with zero mean curvature

($H = 0$) and negative or vanishing Gaussian curvature ($K \leq 0$). Hence, TPMS are saddle-shaped everywhere, except at some isolated points where the surface is locally flat ($K = 0$). The specific curvature characteristic is part of the reason why TPMS have attracted interest as templates for tissue engineering scaffolds, since surface curvature is known to control the organization and dynamics of tissues and cells.^[24] We quantified the curvature distributions of the P and G unit cells, as well as that of their skeletonized variants that are obtained at $\phi_h = 0.2$ and $\phi_s = 0$ (Figure 3a). We found that the “46” and “26” skeletonized designs of the P and G surfaces are, on average, less intrinsically curved than the “24” designs. Indeed, the P_{46} , P_{26} , G_{46} , and G_{26} designs all maintain the locally flat regions in the skeletonized representations. These flat regions are connected through weakly or strongly curved ribbons in the “26” and “46” designs, respectively. In the P_{24} and G_{24} designs, however, the

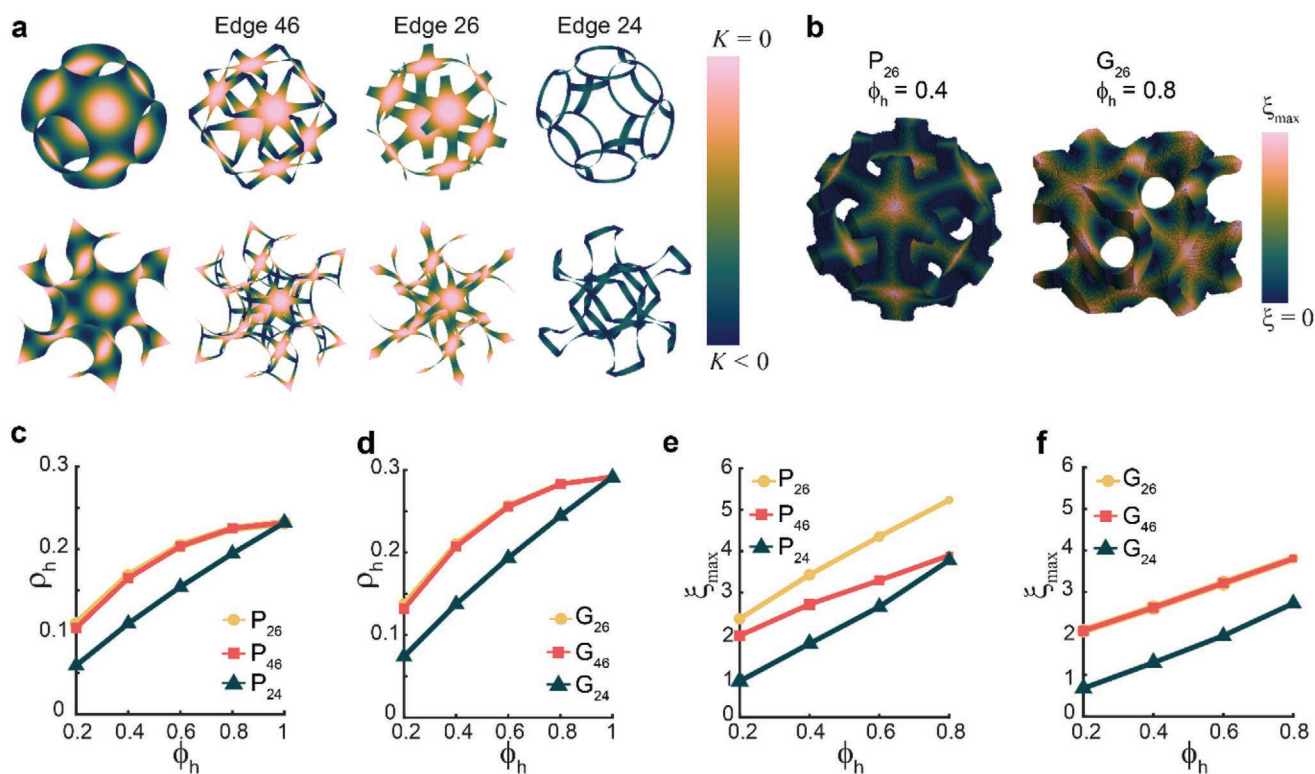


Figure 3. Morphology of TPMS-based metamaterials. a) The Gaussian curvature distribution of the P and G surfaces, as well as their different skeletonized representations. b) The visualization of the shell factor ξ for the P_{26} (left) and G_{26} (right) designs with $t = \frac{L}{10}$. c,d) The hard-phase volume fraction (ρ_h) versus the offset parameter (ϕ_h) for different designs with a shell thickness of $t = \frac{L}{10}$, for the P and G surfaces respectively. e,f) The maximum shell factor (ξ_{max}) versus the offset parameter (ϕ_h) for different designs with a shell thickness of $t = \frac{L}{10}$, for the P and G surfaces respectively.

flat regions are absent and the skeletonized representation consists entirely out of highly curved ribbons (Figure 3a).

As mentioned before, the surfaces are converted to sheet-solids by offsetting the surface in both normal directions by a desired amount. This thickening operation, combined with variations in ϕ_s and ϕ_h , enabled us to achieve a wide range of metamaterial volume fractions ρ . Here, $\rho = V_{solid}/L^3$, where V_{solid} is the volume of the solid material and L is the width of the cubic bounding box (Figure 2a). We quantified the scaling of ρ_h , that is, the volume fraction of the hard phase, with respect to the offset parameter ϕ_h , finding that the “26” and “46” designs follow the same nonlinear scaling law in both the P (Figure 3c) and G (Figure 3d) surfaces. In the “24” designs, an almost linear relation between ϕ_h and ρ_h is observed, with lower values of ρ_h than in the “26” and “46” designs for $\phi_h < 1$. Indeed, the soft phases in the P_{24} and G_{24} designs are always larger for a given value of ϕ_h (provided $\phi_h < 1$) than in the other designs of the same family (Figure 2c,d). Since these plots were made at constant shell thickness (t), these relations also approximate the scaling of the surface area with ϕ_h ($S_{solid} \approx 2 \cdot \frac{V_{solid}}{t}$). Hence, for a fixed value of ϕ_h , these plots indicate that the total surface area is lower in the “24” designs. This is because the “24” skeleton designs do not contain the locally flat mesh regions (Figure 3a), which are the largest contributors to the overall unit cell area. Specifically, if the Enneper–Weierstrass map is

applied to a uniformly-meshed integration domain with equal-area triangles, then the corresponding fundamental patch triangles in the regions with small Gaussian curvature will have larger area than the triangles in regions with strongly negative Gaussian curvature (Figure 2a). Indeed, the area element of the P and G minimal surfaces at a local point is inversely related to the Gaussian curvature at that point (Experimental Section).

The continuous hard phase of our biphasic metamaterials, which forms the reinforcing backbone of the entire unit cell, interpolates between a strut-like (low ϕ_h) and shell-like (high ϕ_h) nature. In order to characterize this behavior, we introduced a shell factor ξ . We defined ξ for any point in the hard phase as the shortest distance to the soft phase, divided by the shell thickness of the unit cell (Experimental Section). As such, ξ is a measure of the largest circular shell that locally fits inside the hard phase at every point, with larger ξ representing a locally more shell-like morphology. We quantified ξ_{max} for the P and G designs (Figure 3b,e,f) as a function of the offset factor ϕ_h . As a consequence of its specific definition, using the distance to the soft phase, the metric ξ is not defined at $\phi_h = 0$. Therefore, we have only plotted ξ_{max} versus ϕ_h for the range that corresponds to the biphasic designs considered in Figure 2c,d (i.e., $\phi_h \in [0.2, 0.8]$). All the three P designs exhibited a different scaling of ξ_{max} with ϕ_h , while the G_{26} and G_{46} showed the same scaling behavior. Moreover, the P_{24} and G_{24} designs achieved the lowest values for ξ_{max} , indicating a more strut-like morphology across the

range of φ_h . This is the consequence of the selective removal of flat regions in these designs (Figure 3a).

2.4. Fluid Permeability

We were interested in the fluid permeability of the different metamaterial designs, as this is an important property in various applications. In tissue scaffolds, for example, permeability affects the supply of nutrients and oxygen to cells, the ingrowth of regenerated tissue, and the potential biodegradation behavior of the scaffolds.^[25] Therefore, we estimated the effective intrinsic permeability using a lattice-Boltzmann simulation scheme (Experimental Section). The permeability is entirely determined by the unit cell geometry, and is independent of the shape and size of the partitioned domains. For example, all P designs in Figure 2c would exhibit the same permeability as their overall geometry is that of the standard P surface. Therefore, the only parameters affecting permeability are the design type, the shell thickness, and the total offset parameter $\varphi = \varphi_h + \varphi_s$. Since our primary interest lies with metamaterials that have critical radii roughly in the order of $10^1 - 10^4 \mu\text{m}$, the effects of surface hydrophilicity on fluid permeability can be considered negligible, as the fluid boundary layer is much smaller than the pores through which the fluid passes. For applications at the nanometer scale, such as membranes for filtration, these effects might play a role on the overall fluid permeability and could be taken into consideration by implementing (partial) slip boundary conditions in the simulations.^[26]

As expected, the normalized effective permeability k^*/L^2 decreases with the volume fraction ρ (Figure 4a), following a similar trend for all designs. Moreover, the permeabilities of the designs based on the G surface are consistently lower than those of the P surface designs. This has previously been observed for full P and G designs, and was attributed to the lower specific surface area of the P surface.^[27] While permeability clearly scales inversely (and nonlinearly) with the volume fraction, it is not the only geometric parameter of relevance. We find that the permeability values scale almost linearly with $\frac{(1-\rho)^3}{(S/L^3)^2}$, where S is the surface area of the unit cell and L is the bounding box width (Figure 4b,c). This factor also appears in the so-called Kozeny equation for predicting the permeability

of porous materials, and indicates that the specific surface area (S/L^3) also plays a role in dictating the metamaterial permeability.^[25,27]

2.5. Elastic Mechanical Properties

The other set of key properties of interest in this study are the elastic mechanical properties, which depend not only on the unit cell geometry (i.e., ρ , φ , and t) but also on the bulk properties of both materials. We computed the effective elastic properties of the resulting designs using a computational homogenization scheme (Experimental Section). Through this finite element-based approach, we calculated the effective stiffness tensor \mathbf{C}^* for every design, from which properties, such as the effective elastic modulus (E^*), bulk modulus (K^*), shear modulus (G^*), and Poisson's ratio (ν) could be obtained (Experimental Section).

The effective elastic modulus E_{11}^* of the uniphase skeleton and full structures, which is defined as their stiffness under uniaxial loading in the direction $\langle 100 \rangle$ and is calculated for $\varphi = \{0.2, 0.4, 0.6, 0.8, 1\}$ and $t = \{L/20, 2L/20, 3L/20\}$, scaled according to a power law of ρ (Figure 5a), as expected from the well-known Gibson–Ashby relationships.^[28] The weakest structures corresponded to the strut-like P_{24} and G_{24} designs with an offset parameter of $\varphi = 0.2$ and a shell thickness of $t = \frac{L}{20}$.

All of our strut-like designs (i.e., those with low φ), correspond to bending-dominated architectures according to the Maxwell–Calladine criterion, indicating sub-optimal stiffness.^[29] The stiffest structures, corresponding to G-based shell-like architectures ($\varphi \geq 0.8$), achieved specific stiffness values close to the Hashin–Shtrikman upper bound (HSU) for nearly isotropic structures, which was also the case for the bulk and shear moduli (Figure S1a,b, Supporting Information).^[5b] It is, however, important to realize that the priority in (and the novelty of) this study is achieving high tunability in mechanical and mass transport properties, rather than presenting new geometries that achieve extreme (specific) properties. Finally, we also observed positive effective Poisson's ratios for all designs (Figure S1c, Supporting Information).

The central concept of our design approach is the ability to parametrically partition the unit cells into two distinct domains. As such, we are able to tune the mechanical properties using

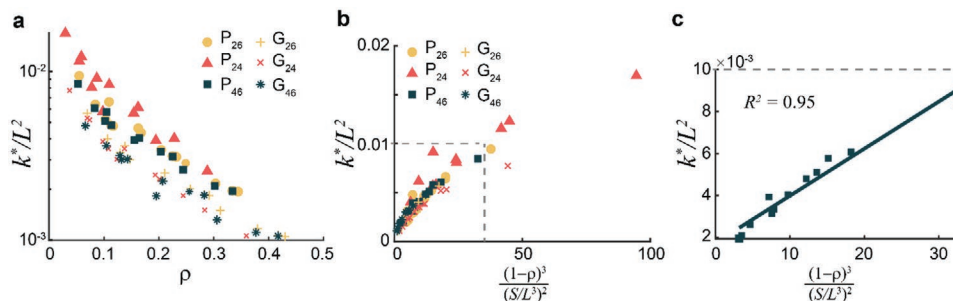


Figure 4. Fluid permeability of TPMS-based metamaterials. a) The normalized effective permeability (k^*/L^2) versus volume fraction (ρ) for full and skeleton P and G designs. b) k^*/L^2 versus the geometric factor $\frac{(1-\rho)^3}{(S/L^3)^2}$ for all the designs in (a). c) A magnified view of the data for the P_{46} designs in (i).

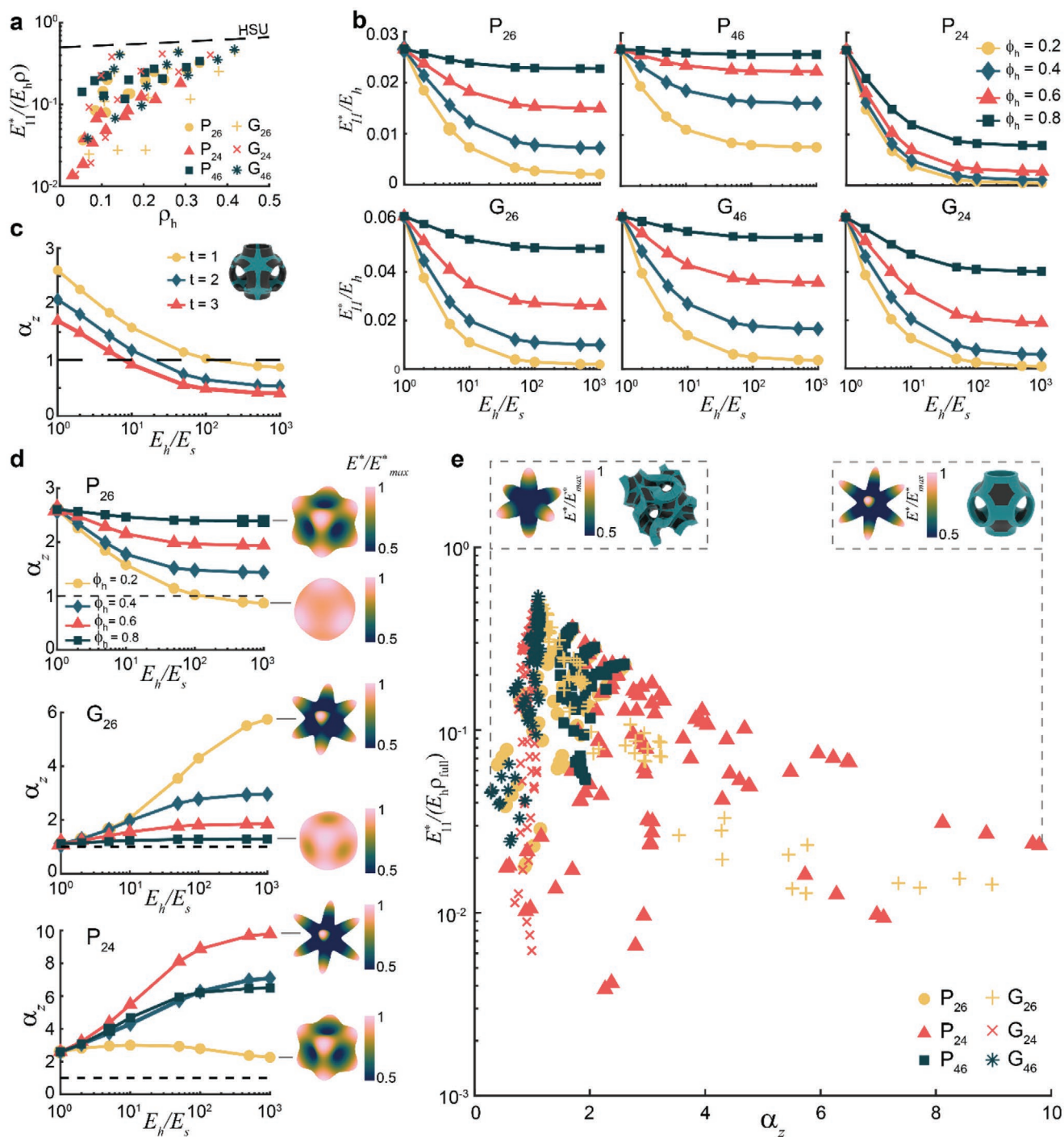


Figure 5. The elastic mechanical properties and anisotropy of TPMS-based metamaterials. a) The normalized effective elastic modulus for uniphase full and skeleton designs ($\varphi_s = 0$, $\varphi_h = \varphi \in [0.2, 1]$, $t \in [\frac{L}{20}, \frac{3L}{20}]$). The HSU-line indicates the Hashin–Shtrikman upper bound. b) The effective stiffness versus the ratio of the Young’s moduli of both phases (E_h/E_s) for the six full biphasic design types with $t = L/20$ and $\varphi_s = 1 - \varphi_h$. c) The Zener anisotropy index (α_z) versus E_h/E_s for the full P_{24} design with different thicknesses. d) Some examples of the scaling of α_z with E_h/E_s for the different amounts of the hard phase (φ_h) in the full P_{26} (top), G_{26} (middle), and P_{24} (bottom) designs. The inset figures on the right represent the effective elastic surface (effective modulus in all directions). All curves are for $t = \frac{L}{20}$. e) The normalized effective stiffness versus Zener anisotropy index for the full designs (with $\varphi_h \in [0.2, 1]$, $\varphi_s = 1 - \varphi_h$, $t \in [\frac{L}{20}, \frac{3L}{20}]$ and $\rho_{full} = \frac{V_h + V_s}{L^3}$). The inset figures show the elastic surfaces and unit cells for both extremal designs regarding α_z . All simulations were performed with $E_h = 2$ GPa and $\nu = 0.3$.

a combination of geometry and material distribution. To study the effects of material choice, we plotted the effective stiffness against the ratio of the Young's moduli of the hard and soft materials (E_h/E_s) for all six design types, with $\phi_h \in [0.2, 0.8]$ and $\phi_s = 1 - \phi_h$ (Figure 5b). When $E_h/E_s = 1$, the behavior of the standard uniphase P or G unit cell is obtained. For increasing values of E_h/E_s , the stiffness reduces for all six design types. As expected, this stiffness reduction is much stronger for the lower values of ϕ_h , where the proportion of the hard phase is low. For example, the stiffness of the P_{26} design with $\phi_h = 0.8$ and $E_h/E_s = 10^3$ is 15% lower than at $E_h/E_s = 1$, while it is 92% lower when $\phi_h = 0.2$ (Figure 5b). Moreover, in all designs, the stiffness reduction curves flatten out when $E_h/E_s \approx 100$. Beyond this point, the soft phase hardly contributes to the overall stiffness, and the load is primarily carried by the hard phase, which forms a reinforcing skeleton for the overall unit cell. Additionally, the stiffness reduction behavior varies among the different designs. For the same values of ϕ_h , the P_{24} and P_{46} designs exhibit the highest and lowest reduction behavior, respectively. This could be attributed to the overall geometry of the hard phase in both cases: the P_{24} skeleton consists entirely out of highly-curved, slender struts, while the P_{46} skeleton contains a higher number of struts, which are approximately straight and, hence, more efficiently carry load (Figure 3a). It is noteworthy that both phases could also be reversed, resulting in biphasic metamaterials with a soft-phase continuous skeleton and disconnected hard-phase inclusions. In such designs, however, the soft phase would form the primary load-carrying component and the hard-phase inclusions would contribute much less to the overall load transfer. This results in rapid and drastic reductions in the effective stiffness as E_h/E_s increases, and also leads to a loss of stiffness tunability for large values of E_h/E_s (Figure S2, Supporting Information). Hence, we only consider the designs with a continuous hard-phase load path in the remainder of this study.

The elastic properties of metamaterial architectures are, in general, anisotropic, though isotropic variants have been proposed.^[5a] We quantified the elastic anisotropy of the different designs as function of E_h/E_s using the Zener anisotropy index α_Z (Experimental Section). When $\alpha_Z = 1$, the structure is elastically isotropic, meaning that the effective stiffness is equal in all directions. We found that α_Z varies with E_h/E_s and shell thickness t for all the designs, although the extent to which it varies depends on the design type (Figure 4c,d and Figure S1, Supporting Information). For example, the standard, uniphase unit cell of the P designs (obtained at $E_h/E_s = 1$) is anisotropic, with $\alpha_Z > 1$. However, the anisotropy index changes with E_h/E_s for biphasic designs, as exemplified in Figure 5d. In case of the P_{26} design, α_Z remains almost constant throughout the range of material ratios for $\phi_h = 0.8$. In this case, the effective elastic surface, representing the effective stiffness in all directions (Figure 5d), indicates a higher stiffness in the $\langle 111 \rangle$ direction as opposed to the $\langle 100 \rangle$ direction. However, for $\phi_h = 0.2$, α_Z rapidly reduces with increasing E_h/E_s , achieving an isotropic design when $E_h/E_s \approx 10^2$. In the P_{24} design, a large spread in α_Z is observed for the different values of ϕ_h , especially for the larger values of E_h/E_s . At $\phi_h = 0.2$, the anisotropy of this design remains almost constant throughout the range of E_h/E_s . However, larger anisotropies are obtained for $\phi_h > 0.2$, with

the maximum being reached for the designs with $\phi_h = 0.6$. Hence, the elastic anisotropy of the P_{24} design is highly sensitive to the interplay between the amounts of the hard and soft phases on the one hand, and the ratio of the Young's moduli of both materials on the other hand. Contrary to the P designs, the G designs start off as quasi-isotropic structures for $E_h/E_s = 1$. For the G_{26} design specifically, an increase in α_Z was observed as E_h/E_s increased, in particular when $\phi_h = 0.2$ (Figure 5d). To summarize the elastic property space, we plotted the normalized effective modulus versus the Zener anisotropy index (Figure 5e). We found that most anisotropic designs have $\alpha_Z > 1$, although some designs (e.g., for G_{46} and P_{26}) exhibited $\alpha_Z < 1$. The largest spread in anisotropies were found in the G_{26} and P_{24} designs, the latter reaching a maximum of $\alpha_Z \approx 10$. Moreover, we observed a relatively large number of designs in the quasi-isotropic range ($\alpha_Z \approx 1$), which cover approximately two orders of magnitude in the effective stiffness. Overall, these results confirm that our metamaterial design strategy not only enables the effective tuning of the uniaxial stiffness, but also of the elastic anisotropy. While others have observed large (and non-monotonic) anisotropy variations in uniphase metamaterials at different volume fractions,^[7d] our anisotropy ranges are obtained for constant overall unit cell geometry and volume fraction.

2.6. Balancing Elasticity and Permeability

Our parametric design approach substantially enhanced the ability to independently tailor the mechanical and mass transport properties of TPMS-based metamaterials. This is visualized in the elasticity-permeability property space, where the effective elastic modulus normalized by the hard-phase elastic modulus (E^*/E_h) is plotted against the intrinsic (area-normalized) effective permeability (k^*/L^2) for all uni- and biphasic designs (Figure 6a). In the case of the "full" unit cells (i.e., the unit cells with the standard P or G morphology, $\phi_s = 1 - \phi_h$), the biphasic partitioning unlocks a wide range of attainable stiffness values for a constant value of permeability (the data points in the yellow bands in Figure 6a). Indeed, for those designs, the permeability is only determined by the overall unit cell type (P or G) and shell thickness (t), while the stiffness is also driven by the material distributions. The maximum stiffness for the full designs is, not surprisingly, obtained for $\phi_h = 1$ (i.e., unit cells that consist entirely out of the hard phase).

While biphasic partitioning enables continuous stiffness tuning in standard TPMS unit cells, their intrinsic permeability range is still limited and is only a function of the shell thickness (t). However, the range of intrinsic permeability values is extended by the skeleton TPMS structures ($\phi_h + \phi_s < 1$), which have more holes in their surfaces, thereby altering the fluid flow through the unit cell. Indeed, all data points outside of the yellow bands in Figure 6a correspond to uni- or biphasic skeleton designs. Similar to the case of full designs, using two different materials in the skeleton designs enables the tuning of the elastic properties independently from permeability. Alternatively, one could fix the effective normalized stiffness and tune the permeability by choosing a different design at the same level of stiffness. We note that we have visualized

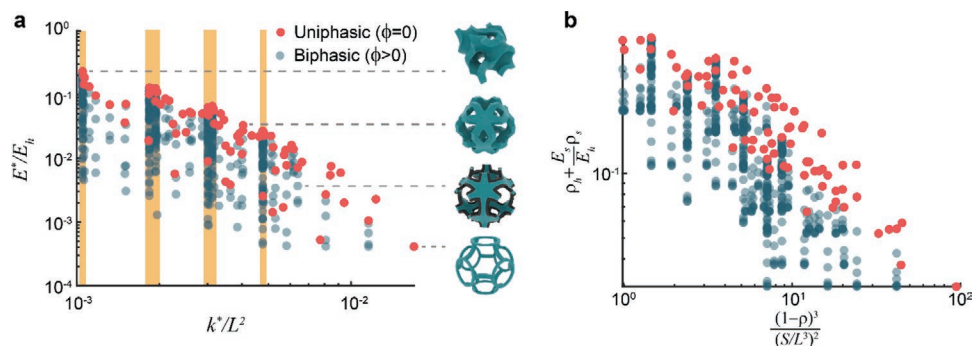


Figure 6. Effective stiffness versus effective permeability. a) The normalized effective elastic modulus versus the normalized effective permeability for uni- and biphasic designs. The yellow bands indicate the “full” designs (i.e., $\varphi_s + \varphi_h = 1$). The unit cell structures belonging to four data points are visualized in the inset figures. b) Simple scaling laws that capture the behavior from (a). The elastic properties are determined by the geometry and materials choice, captured by $\rho_h + \frac{E_s}{E_h} \rho_s$ while the permeability depends on the geometry alone, as described by $(1 - \rho)^3 / (S/L^3)^2$.

the elasticity-permeability design space using discrete values of t , φ_h , φ_s , and E_h/E_s in Figure 6, and that intermediate data points could be obtained at intermediate values of the design parameters.

Our design approach enables this level of mechanical and mass transport tunability by leveraging the fact that permeability solely depends on geometry, while the elastic properties depend on geometry and material choice. To further demonstrate this, we plotted $\rho_h + \frac{E_s}{E_h} \rho_s$ against $\frac{(1-\rho)^3}{(S/L^3)^2}$ (Figure 6b), which captures the same trend as in the elasticity-permeability map. The former quantity captures the combined effect of the geometry and material properties on the effective stiffness: the stiffness is primarily determined by the volume fraction of the hard phase, while the soft phase has a weighted contribution, depending on its stiffness relative to the hard phase. The second quantity $\left(\frac{(1-\rho)^3}{(S/L^3)^2}\right)$ is the purely geometry-dependent

metric that was introduced before (Figure 4b,c) and that correlates with the permeability. Taken together, these results summarize our enhanced ability to tune elasticity and permeability independently, by combining spatial distribution of multiple materials with geometric control over the unit cell architecture.

2.7. Multi-Material Additive Manufacturing

We physically realized metamaterial lattices based on the P surface, using multi-material additive manufacturing (Experimental Section). The lattices consisted of 27 unit cells, in a $3 \times 3 \times 3$ arrangement (Figure 7a). We printed two uniphase full designs in a hard (top left in Figure 7a) and soft (bottom right in Figure 7a) polymer, as well as a uniphase P_{46} skeleton design ($\varphi_h = 0.2$, $\varphi_s = 0$, top right in Figure 7a), and a biphasic P_{46} design ($\varphi_h = 0.2$, $\varphi_s = 0.8$, bottom left in Figure 7a). All structures were successfully printed, and showed no signs of

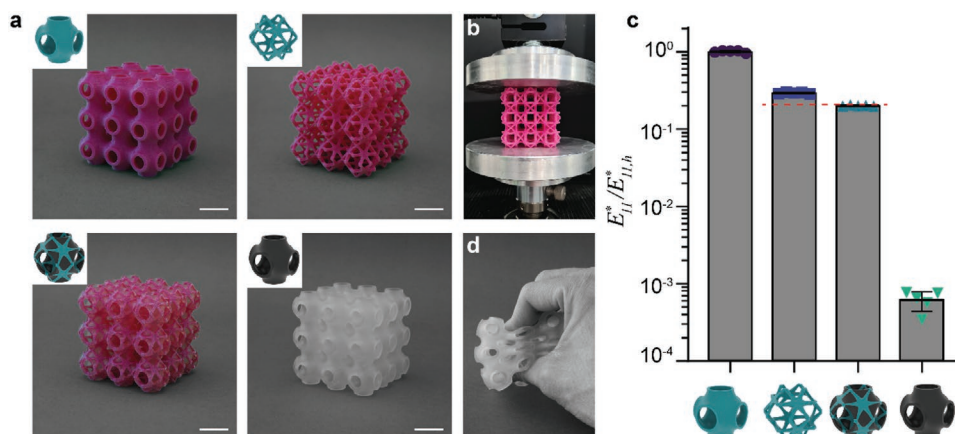


Figure 7. Additively manufactured structures and mechanical testing. a) Lattices consisting of 27 unit cells fabricated using multi-material polymer printing. The pink material is a stiff polymer (VeroMagenta), while the white transparent material is soft (Agilus30) and easily deformable. b) The mechanical testing of the 3D-printed structures using a displacement-controlled compression test setup. c) Normalized compression testing results for the four printed specimens, showing the uniaxial effective modulus. Each test was repeated five times. The markers show the individual test results, while the bar graph represents the mean and standard deviations. The red dashed line corresponds to the predicted stiffness for the uni- and biphasic skeletons. d) The structure that consists entirely out of the soft phase is highly deformable and has a negligible stiffness as compared to the other designs. Scale bars represent 20 mm.

defects. In the case of the biphasic design, the soft phase was well integrated with the hard-phased skeleton.

We mechanically tested the specimens by imposing a small macroscale compressive strain (Figure 7b and Experimental Section), in order to examine the effective elastic modulus. Compared to the fully hard structure, the stiffness of the skeletonized structures (uni- and biphasic) was 70–80% lower, while the stiffness of the fully soft structures was three orders of magnitude lower (Figure 7c,d). We observed that the stiffness reduction in the biphasic design corresponded well with the computationally predicted stiffness reduction (dotted line in Figure 7c). However, the stiffness of the uniphase skeleton was higher than that of the corresponding biphasic design, while their predicted stiffness values are equal. This difference could be due to the differences between the load-carrying hard phases present in both designs. Due to the localized mixing of the polymer droplets in the material jetting process, the transition regions of the hard and soft phases in the biphasic designs are expected to possess different material properties than the uniphase skeleton designs. This could mean that the main load-carrying phase is, effectively, narrower in the biphasic design. In another study on interpenetrating phase composites, fabricated using the same printing process, the quality of the interface between the hard and soft polymers was suggested as a key factor governing the overall mechanical properties of the resulting materials.^[30] While initial microscopic investigations of our samples seemed to indicate slightly narrower hard-phase regions in the biphasic structure (Figure S3, Supporting Information), more conclusive evidence would be needed to confirm this. For example, indentation testing of the material properties in and around the transition region could shed light on the variations in the local properties, while advanced imaging techniques could provide quantitative insight into the deviations between the 3D designs and the fabricated structures. While these investigations are beyond the scope of this study, these printed lattices nevertheless demonstrate that the biphasic TPMS-based metamaterials can be successfully manufactured using commercially available printing processes.

3. Discussion

We have presented an approach to parametrically design multifunctional metamaterials in which the mechanical and mass transport properties can be decoupled to a large extent. The ability to independently tailor such properties is relevant in many applications. However, not much progress has been made in this direction, particularly using uniphase metamaterials. In a recent work on metallic pentamode metamaterials, the ability to decouple the effective stiffness from the overall relative density was demonstrated, albeit for a small range of densities. While not directly studied, this result implied that the permeability of a given pentamode metamaterial could be tuned (by tuning relative density) without affecting its stiffness.^[15] However, the design space for these metamaterials is very narrow, requiring a highly specific strut-based architecture, and the permeability can only be decreased for any given design with a fixed set of mechanical properties. A different approach that is more generally applicable to strut-based metamaterials

relies on disconnecting struts at random nodes throughout the structure (e.g., splitting four-degree nodes into two separate two-degree nodes^[31]). This splitting operation enabled a reduction in the effective stiffness of almost one order of magnitude, without significantly affecting the permeability, since very little material is removed. However, randomly splitting of vertices throughout the metamaterial lattice may introduce undesired local weaknesses that affect the overall failure behavior. Additionally, this splitting approach is currently only established for strut-based metamaterials with four-degree nodes. Finally, scaling the unit cell dimensions allows for tuning the absolute permeability independently from the elastic properties.^[12c] As previously stated, such a unit cell scaling approach is not always desirable given that it makes it difficult, if not impossible, to keep the other properties of porous materials (e.g., surface area, manufacturability, or pore size) unchanged. Our design approach, on the other hand, partitions the P and G TPMS unit cells into hard, soft, or void domains, effectively resulting in hybrid strut-shell-based metamaterials. By combining the effects of geometry and different bulk materials, we showed that these biphasic decorations offer a wide design space of decoupled effective elasticity and intrinsic permeability. For the same values of the permeability, our approach offers an admissible range of stiffness values that spans several orders of magnitude (bound by properties of the fully hard and fully soft designs). Additionally, our approach offers a route to tailor the elastic anisotropy of the structure (while maintaining cubic symmetry). While our analyses were performed for various shell thicknesses, we did not explore through-the-thickness material variations in this work. This is because our biphasic decorations were designed using the “zero-thickness” surface definition of the fundamental patch, which was subsequently patterned to create a translational unit cell and thickened to obtain a solid geometry. As an extension to our approach, a through-the-thickness variation in the material properties could be considered. For example, the unit cell could be designed to have a hard-phase core with a thickness t_h sandwiched between soft-phase layers with a thickness t_s , resulting in an overall shell thickness of $t = t_h + 2t_s$, which is similar to core-shell cellular composites.^[32] For sufficiently high values of E_h/E_s , this could also enable a decoupling of the elastic properties from t , and, thus, the fluid permeability. For a given unit cell geometry (i.e., for a constant permeability), the theoretical range of attainable stiffness values remains unchanged regardless of whether our approach is used or through-the-thickness material variations are introduced, because the extremal values for E^* are obtained for a fully soft and fully hard design. However, the through-the-thickness biphasic decorations may be more challenging to physically realize with multi-material printing particularly for the smaller values of t , due to the existing limitations regarding the printing resolution.

While we have focused on the quasi-static elastic properties here, it is likely that the combination of hard and soft phases would also affect the other mechanical properties of TPMS-based architectures, including those pertaining to dynamic loading. For example, the presence of soft inclusions within the hard load-carrying skeleton may enhance the fracture toughness and improve the overall fatigue and energy absorption behavior of the resulting materials.^[32,33] Moreover, the

viscoelastic behavior of the soft phase could affect the strain-rate dependent properties of the overall metamaterial: at a high loading rate, the soft phase would be expected to act as a stiffer material and carry more load as opposed to a low (i.e., quasi-static) loading rate. Additionally, the combination of two materials with different strain rate-dependencies could affect the overall metamaterial deformation mode at different loading rates, as we have recently demonstrated using the same multi-material printing technique that was employed in this study.^[34] The elastic deformability of the soft inclusions within the load-carrying phase could also affect the post-failure response and damage tolerance of the overall lattice, by improving the recovery of the original geometry after load removal, and by preventing the catastrophic disintegration of the lattice after the failure of the hard phase.^[35] These mechanical properties could be experimentally investigated in future research. Additionally, the fluid permeability of the different designs could be experimentally tested in future studies. Several setups have been devised to quantify the fluid permeability of architected materials, such as tissue scaffolds.^[36] Typically, these methods require placing the structure in a column with a flowing fluid (typically water) and measuring the fluid mass flow rate or pressure drop across the structure. The fluid permeability is then determined by applying the Darcy's law, making sure the Reynolds number (Re) remains sufficiently low (typically $Re < 10$).^[25] The simplest permeability setups make use of a falling-head approach, where a tall column of water is placed above the porous structure and is allowed to flow through it under the action of gravity.^[12b] More advanced methods make use of a constant-head column (i.e., a column that is filled so that the height of the water remains constant) or use a peristaltic pump to force the liquid through the scaffold.^[25,36,37]

Our approaches could be generalized and extended in various ways. First, it would be possible to vary the unit cell type throughout the metamaterial lattice, for example, to spatially vary the permeability without affecting the local elastic properties. This could be achieved by fixing the geometry of the hard phase in all the unit cells, but varying the amount of the soft phase (Figure S4a, Supporting Information). Alternatively, the overall unit cell geometry could be preserved, hence fixing permeability, but the elasticity could be spatially tuned by varying the amount of the load-carrying hard phase (Figure S4b, Supporting Information). Our approach could also be extended to enable other types of shell-based biphasic metamaterials. For example, the same hyperbolic tilings that we have used here could be projected onto the D (diamond) minimal surface, which belongs to the same family as the P and G surfaces (Figure S5, Supporting Information). We did not include the D designs in this study, as these unit cells contain non-manifold regions where different patches meet along single edges, rendering them unattractive from a mechanical viewpoint. Moreover, many other biphasic P and G designs could be created, beyond the ones we have presented here. For example, the tilings that we have used could be combined together to form hybrid structures (Figure S6, Supporting Information). Alternatively, many other tilings exist that could be projected onto these cubic TPMS to make different admissible biphasic designs.^[20a,c] In addition to the PDG surface family of minimal surfaces, our design approach could readily be extended

to other TPMS families, provided their Enneper–Weierstrass parametrization is known. The Weierstrass function has already been determined for several other TPMS families, but can also be uncovered for newer types of TPMS on the basis of the local flat points, which could be determined numerically.^[38] Finally, the central concept of decorating a lattice with two (or more) different materials could also be applied more generally to other metamaterial architectures.^[39] For example, hard-phase nodes and soft-phase struts have been combined to program buckling-driven deformation modes in strut-like metamaterials.^[17b] However, a disadvantage of such designs is that there is no continuous hard-phase load path throughout the metamaterials, making the effective mechanical properties strongly dependent on the properties of the soft phase. Our approach, on the other hand, enables the parametric design of distinct, continuous hard-phase load paths within the predominantly soft shell-based TPMS metamaterials, which, for large enough values of E_h/E_s (e.g., $E_h/E_s \approx 1000$), fully control the effective elastic properties of the overall metamaterial. In principle, these embedded hard-phase load paths could also be defined in other bicontinuous shell-based geometries, such as stochastic spinodoids, which have recently emerged as attractive metamaterial designs.^[6d,40] However, those other designs are not compatible with the straightforward Enneper–Weierstrass parametrization and the projection of hyperbolic tilings that we have leveraged in our technique, and would require a different strategy to spatially distribute the different phases. A potential strategy could be to use a parametric skeletonization algorithm to obtain the medial graph of the shell-based structure,^[41] and to assign material properties to this region that are different from the remainder of the geometry.

Biphasic metamaterials with decoupled permeability and mechanical properties could be useful in several applications, such as in the development of architected, porous scaffolds for tissue engineering. These scaffolds require a delicate balance between tissue-mimicking mechanical properties and mass transport properties to facilitate oxygenation and nutrient transport, and to enable tissue ingrowth.^[16,25,31,42] The competition between these properties forms a central challenge in scaffold design, but our approach could offer an attractive route towards optimizing the scaffolds for both sets of properties independently. Additionally, the use of two different materials could enhance the overall biological functionality, since one material could be optimized for load transfer, while the other could be optimized for cell interactions (e.g., through the controlled release of drugs^[43]). Other applications that rely on cellular materials for fluid transport could also benefit from the presented design approach, as these materials may also need to carry some mechanical loads. In such cases, our approach could enable increased design freedom to tailor the fluid permeability, while still satisfying structural requirements. Examples are porous materials in the trailing edges of airplane wings or wind turbine blades for noise-mitigation purposes, or TPMS-based heat exchangers, filtration systems, and catalytic substrates in load-carrying configurations.^[7a,44] Beyond fluid permeability, the ability to decouple mechanical properties from the overall pore architecture may also inspire future (small-scale) metamaterials used for energy storage, photonic, or acoustic applications.^[45] If the mechanical properties are not critical, the two materials of

our biphasic metamaterials could be tuned for different properties, such as the simultaneous optimization of thermal and electrical conductivities.^[10] For example, the hard-phase skeletons that served as continuous load paths in our work might act as a template for 3D electrical circuits embedded in TPMS-based metamaterials.

From a broader perspective, this study underscores the relevance of reticular (or structural) chemistry as a source of inspiration for metamaterial design. In addition to the hyperbolic networks described here, there are vast databases of complex topologies that could be used as metamaterial templates.^[21] For example, the wealth of zeolitic networks and metal–organic frameworks (MOFs) could inspire complex designs that go beyond the traditional lattice choices (e.g., cubic or diamond lattices), resulting in so-called “meta-MOFs”.^[46] Moreover, metamaterial properties could be enhanced even further by incorporating the same hardening mechanisms that are found at the atomic scale in crystalline materials.^[47]

Taken together, we demonstrated a new strategy for the multi-objective design of multi-physics metamaterials and a route to decouple properties that are conflicting in uniphase metamaterials. By leveraging the hyperbolic symmetries of TPMS, our design approach maintains a surprising tractability, yet produces complex 3D, biphasic architectures. Together with advances in multi-material additive manufacturing, this design approach could unlock exciting routes towards multi-physics metamaterials in a variety of applications. In this regard, we believe that decoupling elasticity and permeability is only one example of the potential for enhanced tunability in biphasic metamaterials.

4. Experimental Section

Parametric Design of TPMS: The 3D mesh representations of the labelled P and G surfaces were computed using the Enneper–Weierstrass parametrization, which maps the points in an integration domain in the complex plane to the curved fundamental patch in \mathbb{E}^3 that was used to build the TPMS. Specifically, the Cartesian coordinates of the points on the fundamental patch were obtained by:

$$\begin{Bmatrix} x \\ y \\ z \end{Bmatrix} = \operatorname{Re} \left[e^{i\theta} \begin{Bmatrix} \omega \\ \omega_0 \end{Bmatrix} \begin{Bmatrix} 1 - \bar{\omega}^2 \\ i(1 + \bar{\omega}^2) \\ 2\bar{\omega} \end{Bmatrix} \right] R(\bar{\omega}) d\bar{\omega} + p_0 \quad (1)$$

Here, $R(\bar{\omega})$ is the Weierstrass function, θ is the Bonnet angle, p_0 is an arbitrary translation to define the origin (here, $p_0 = [0, 0, 0]$), ω_0 is a fixed point in the integration domain (here, $\omega_0 = 0$), and ω is any other point in the integration domain. For the PDG surface family, the Weierstrass function is defined as:

$$R(\bar{\omega}) = [\bar{\omega}^8 - 14\bar{\omega}^4 + 1]^{\frac{1}{2}} \quad (2)$$

For the P surface, $\theta = \frac{\pi}{2}$. For the G surface, $\theta = \arccot \left(\frac{E_k \left(\frac{3}{4} \right)}{E_k \left(\frac{1}{4} \right)} \right)$, where

$E_k(k)$ is the complete elliptic integral of the first kind with parameter k . Thus, any point ω in the complex domain is mapped to a point in the 3D fundamental patch through this parametrization. The points ω were

uniformly sampled from the complex domain, depending on the patch type and the desired density. In case of the P_{46} design, for example, all points were sampled from parallel lines to the “46” edge of the complex domain. Next, the Delaunay triangulation of the set of discrete points ω was computed to obtain a triangular (2D) mesh of the complex domain (Figure 2a). The faces of the 2D mesh were labelled as hard, soft, or void phase (in parallel bands), depending on the desired offset parameters φ_h and φ_s (Figure 2a). The Enneper–Weierstrass equations were then used to map the points ω to their Cartesian coordinates in \mathbb{E}^3 . The mesh topology and face labelling that was computed on the 2D complex domain was applied to the 3D set of points to obtain a meshed representation of the fundamental patch. Finally, the patch was patterned in 3D according to the P and G symmetry operations to obtain the translational unit cells.^[23]

All computations and consequent mesh processing steps were performed in MATLAB (MATLAB 2018b, Mathworks, Natick, MA, USA) using custom code, as well as by using several of the functions of the GIBBON toolbox.^[48]

Conversion to Solid Structures: The zero-thickness meshes were converted to solid, 3D-printable structures by a surface thickening approach. To this end, all vertices were offset in the positive and negative normal directions by a distance $d/2$, where d is a user-defined fraction of the unit cell bounding box width L (i.e., $d = \frac{t}{20}L$). This

offsetting operation resulted in two parallel meshes, one at each side of the original minimal surface mesh. Triangular bounding faces were added at the edges of the two parallel meshes to create a watertight mesh that represents the solid structure. This thickening approach was applied for every labeled region of the mesh separately, resulting in a solid triangle mesh for both the hard and soft phases. The surface area and relative densities were then computed on the basis of these triangle meshes, and the meshes were exported in the STL format for printing and visualization in Keyshot (Keyshot 5, Luxion, Tustin, CA, USA). The voxelized representations of the unit cells were created from the triangle meshes using the function *patch2lm* in the GIBBON toolbox.^[48]

Morphology: The Gaussian curvature (K) of the TPMS mesh vertices (Figure 3a) was computed from the complex domain as:^[49]

$$K(\omega) = -4(1 + |\omega|^2)^{-4} |R(\omega)|^{-2} \quad (3)$$

The area element (dS) or surface metric for a point $\omega = u + iv$ is defined as:^[50]

$$dS = du dv (1 + |\omega|^2)^2 |R(\omega)|^2 \quad (4)$$

The shell factor ξ was computed on the voxelized mesh representations ($100 \times 100 \times 100$ voxels) of the entire unit cell. First, the soft phase of the unit cells was thresholded, resulting in a binary $100 \times 100 \times 100$ array with label 1 for all the voxels in the soft phase, and label 0 for all other voxels. Then, the Euclidean distance map (EDM) was computed on this 3D array, specifying the distance from every voxel to the nearest voxel in the soft phase. The hard phase was then used as a mask to extract the distance of every voxel in the hard phase to the nearest voxel in the soft phase. The distance value was then divided by the local shell thickness to compute the shell factor at every point p in the hard phase (the factor 2 is to obtain the diameter of the largest circular shell that fits inside the hard phase at every point):

$$\xi(p) = 2 \frac{\text{EDM}(p)}{t(p)} \quad (5)$$

Permeability Simulations: The effective fluid permeability for the different uniphase designs was computed using a lattice–Boltzmann (LB) scheme that has previously been used for determining permeabilities of standard TPMS microstructures.^[12c] Briefly, the LB method models the

temporal evolution of a particle velocity distribution function at discrete lattice positions under collision and streaming steps, and subject to a small pressure gradient.^[51] Here, the LB simulations were performed with standard D3Q19 elements (i.e., 3D elements with 19 possible momentum components)^[52] and a lattice discretization of 256³ voxels was used. The intrinsic permeability was extracted using the Darcy's law, and were normalized to the cross-sectional area of the unit cell L^2 .

Effective Elastic Properties: The effective elastic mechanical properties of the different unit cell designs were computed using a computational homogenization scheme based on the finite element method (FEM) in MATLAB.^[53] Briefly, the effective (homogenized) elasticity tensor \mathbf{C}^* (6×6 , using Voigt notation) was extracted from six independent, linear elastic FEM simulations on voxelized representations of the unit cells with periodic boundary conditions. In the simulations, the Poisson's ratio was set to 0.3, and the stiffness of the hard phase was set to 2 GPa. Following a convergence study on the basis of the effective elastic modulus (considered converged when the variation was below 1%), a discretization of the unit cells into 128³ voxels was found to be sufficient to compute the effective elastic properties. The linear force-displacement equations in the FEM simulations were solved using the preconditioned conjugate gradient (pcg) scheme in MATLAB, with a tolerance set to 10^{-8} . Due to the cubic symmetry of the metamaterial designs, \mathbf{C}^* contains only three independent components (i.e., C_{11} , C_{12} , and C_{44}). From those components, the effective uniaxial Young's modulus (E_{11}^* in $\langle 100 \rangle$ direction), effective bulk modulus (K^*), effective shear modulus (G^* ; e.g. applied on the (100) plane in the [010] direction), and the effective Poisson's ratio (ν^* , for loading in the $\langle 100 \rangle$ direction) could be determined^[7d] as:

$$E_{11}^* = \frac{1}{S_{11}^*} \quad (6)$$

$$K^* = \frac{C_{11} + 2C_{12}}{3} \quad (7)$$

$$G^* = C_{44} \quad (8)$$

$$\nu^* = \frac{C_{12}}{C_{11} + C_{12}} \quad (9)$$

Here, S_{11}^* is the (1,1) component of the homogenized compliance tensor \mathbf{S}^* . The Zener anisotropy index for cubic crystals (α_Z) was determined as:^[7d]

$$\alpha_Z = \frac{2C_{44}}{C_{11} - C_{12}} \quad (10)$$

To plot the elastic surfaces (Figure 5d,e), the effective Young's modulus in different directions was calculated by transforming the effective stiffness tensor using the appropriate rotation matrix for every direction.^[53]

The Hashin–Shtrikman (HS) upper bounds for the effective bulk (K_{HSU}) and shear (G_{HSU}) moduli of a nearly isotropic material were computed as:^[5b]

$$K_{\text{HSU}} = \frac{4G_s K_s \rho}{4G_s + 3K_s(1-\rho)} \quad (11)$$

$$G_{\text{HSU}} = \frac{(9K_s + 8G_s)\rho G_s}{20G_s + 15K_s - 6(K_s + 2G_s)\rho} \quad (12)$$

The corresponding HS bound for the Young's modulus (assuming isotropic linear elasticity) was then determined as a function of K_{HSU} and G_{HSU} given by:

$$E_{\text{HSU}} = \frac{9K_{\text{HSU}}G_{\text{HSU}}}{3K_{\text{HSU}} + G_{\text{HSU}}} \quad (13)$$

Multi-Material Additive Manufacturing: Four different designs were additively manufactured through a material jetting process, using a combination of hard and soft photocurable polymer resins. The width of the unit cell bounding box was set to $L = 20$ mm, the shell thickness was $t = 2$ mm, and the lattices consisted of 27 unit cells in a $3 \times 3 \times 3$ arrangement. The fabrication was performed using a Connex3 Objet 350 printer (Stratasys, Minnesota, USA). Both the hard and soft phases were made with commercial polymer resins designed for this printing system: the hard phase was printed using the Veromagenta polymer (Stratasys, $E = 2\text{--}3$ GPa according to the manufacturer), while the soft phase was printed using the translucent, rubber-like Agilus30 polymer (Stratasys, Shore A hardness: 30–35 according to the manufacturer, which corresponds to $E \approx 1.2\text{--}1.4$ MPa using Gent's relation^[54]). This combination of materials has previously been used to print 2D metamaterials with $E_h/E_s \approx 10^3$.^[17c] The lattices were printed with soluble support material (SUP706, Stratasys), which was carefully removed after printing using chemical washing (according to the manufacturer's protocol), water rinsing, and compressed air blowing.

Mechanical Compression Tests: The specimens were mechanically tested in a displacement-controlled uniaxial compression test, using a Lloyd universal test bench (LR5K, Ametek STC, Bognor Regis, UK), equipped with a 5 kN load cell. The test was performed under ambient temperatures (22 °C) at a strain rate of 10^{-3} s⁻¹. A preload of 5 N was used and the test was halted at 2% macroscopic strain. Every specimen was tested five times, allowing ample time between consecutive tests for the material to recover its original shape. Throughout the low-strain testing, the specimens maintained their integrity and the force–displacement curves did not show signs of failure. The effective Young's modulus was determined from the linear-elastic gradient of the linear part of the stress–strain curve.

Supporting Information

Supporting Information is available from the Wiley Online Library or from the author.

Acknowledgements

S. J. P. C. is grateful to Dr. Kevin M. Moerman for helpful discussions and guidance in the use and adaption of the functions in the GIBBON toolbox. The authors are grateful to 3D LifePrints (Oxford, UK) for 3D-printing the specimens shown in Figure 7. The research leading to these results has received funding from the European Research Council under the ERC grant agreement no. [677575].

Conflict of Interest

The authors declare no conflict of interest.

Data Availability Statement

The data that support the findings of this study are available from the corresponding author upon reasonable request.

Keywords

geometries, metamaterial designs, minimal surfaces, multi-material printing

Received: February 8, 2021

Revised: March 13, 2021

Published online: May 4, 2021

- [1] T. Brunet, A. Merlin, B. Mascaro, K. Zimny, J. Leng, O. Poncelet, C. Aristégui, O. Mondain-Monval, *Nat. Mater.* **2015**, *14*, 384.
- [2] J. Pendry, *Science* **2004**, *306*, 1353.
- [3] X. Zheng, H. Lee, T. H. Weisgraber, M. Shusteff, J. DeOtte, E. B. Duoss, J. D. Kuntz, M. M. Biener, Q. Ge, J. A. Jackson, S. O. Kucheyev, N. X. Fang, C. M. Spadaccini, *Science* **2014**, *344*, 1373.
- [4] a) V. S. Deshpande, N. A. Fleck, M. F. Ashby, *J. Mech. Phys. Solids* **2001**, *49*, 1747; b) L. R. Meza, S. Das, J. R. Greer, *Science* **2014**, *345*, 1322; c) J. Bauer, A. Schroer, R. Schwaiger, O. Kraft, *Nat. Mater.* **2016**, *15*, 438; d) C. M. Portela, J. R. Greer, D. M. Kochmann, *Extreme Mech. Lett.* **2018**, *22*, 138.
- [5] a) T. Tancogne-Dejean, M. Diamantopoulou, M. B. Gorji, C. Bonatti, D. Mohr, *Adv. Mater.* **2018**, *30*, 1803334; b) J. Berger, H. Wadley, R. McMeeking, *Nature* **2017**, *543*, 533.
- [6] a) S. C. Han, J. W. Lee, K. Kang, *Adv. Mater.* **2015**, *27*, 5506; b) C. Bonatti, D. Mohr, *J. Mech. Phys. Solids* **2019**, *122*, 1; c) C. Bonatti, D. Mohr, *Acta Mater.* **2019**, *164*, 301; d) C. M. Portela, A. Vidyasagar, S. Krödel, T. Weissenbach, D. W. Yee, J. R. Greer, D. M. Kochmann, *Proc. Natl. Acad. Sci. USA* **2020**, *117*, 5686.
- [7] a) O. Al-Ketan, R. K. A. Al-Rub, *Adv. Eng. Mater.* **2019**, *21*, 1900524; b) O. Al-Ketan, R. Rezugui, R. Rowshan, H. Du, N. X. Fang, R. K. A. Al-Rub, *Adv. Eng. Mater.* **2018**, *20*, 1800029; c) D. Li, N. Dai, Y. Tang, G. Dong, Y. F. Zhao, *J. Mech. Des.* **2019**, *7*, 071402; d) C. Soyarslan, V. Blümer, S. Bargmann, *Acta Mater.* **2019**, *177*, 280; e) S. J. Callens, N. Tümer, A. A. Zadpoor, *Appl. Mater. Today* **2019**, *15*, 453.
- [8] S. Hyde, Z. Blum, T. Landh, S. Lidin, B. W. Ninham, S. Andersson, K. Larsson, *The Language of Shape: The Role of Curvature in Condensed Matter: Physics, Chemistry and Biology*, Elsevier Science, Amsterdam, The Netherlands **1996**.
- [9] a) S. T. Hyde, G. E. Schröder-Turk, *Interface Focus* **2012**, *2*, 529; b) G. E. Schröder-Turk, A. Fogden, S. T. Hyde, *Eur. Phys. J. B* **2006**, *54*, 509.
- [10] S. Torquato, S. Hyun, A. Donev, *Phys. Rev. Lett.* **2002**, *89*, 266601.
- [11] A. A. Zadpoor, *Biomater. Sci.* **2020**, *8*, 18.
- [12] a) H. Montazerian, E. Davoodi, M. Asadi-Eyvand, J. Kadkhodapour, M. Solati-Hashjin, *Mater. Des.* **2017**, *126*, 98; b) F. S. L. Bobbert, K. Lietaert, A. A. Eftekhari, B. Pouran, S. M. Ahmadi, H. Weinans, A. A. Zadpoor, *Acta Biomater.* **2017**, *53*, 572; c) S. C. Kapfer, S. T. Hyde, K. Mecke, C. H. Arns, G. E. Schröder-Turk, *Biomaterials* **2011**, *32*, 6875; d) J. K. Guest, J. H. Prévost, *Int. J. Solids Struct.* **2006**, *43*, 7028.
- [13] M. F. Ashby, *Philos. Trans. R. Soc., A* **2006**, *364*, 15.
- [14] M. Kadic, T. Bückmann, N. Stenger, M. Thiel, M. Wegener, *Appl. Phys. Lett.* **2012**, *100*, 191901.
- [15] R. Hedayati, A. M. Leeflang, A. A. Zadpoor, *Appl. Phys. Lett.* **2017**, *110*, 091905.
- [16] A. A. Zadpoor, *Biomater. Sci.* **2015**, *3*, 231.
- [17] a) S. Janbaz, M. McGuinness, A. A. Zadpoor, *Phys. Rev. Appl.* **2018**, *9*, 064013; b) S. Janbaz, F. Bobbert, M. Mirzaali, A. Zadpoor, *Mater. Horiz.* **2019**, *6*, 1138; c) M. Mirzaali, A. Caracciolo, H. Pahlavani, S. Janbaz, L. Vergani, A. Zadpoor, *Appl. Phys. Lett.* **2018**, *113*, 241903. d) D. Chen, X. Zheng, *Sci. Rep.* **2018**, *8*, 9139; e) S. J. Callens, O. K. Bergsma, *Composites, Part A* **2018**, *114*, 1; f) M. J. Mirzaali, M. Cruz Saldivar, A. Herranz de la Nava, D. Gunashekar, M. Nouri-Goushki, E. L. Doubrovski, A. A. Zadpoor, *Adv. Eng. Mater.* **2020**, *22*, 1901142.
- [18] S. Torquato, A. Donev, *Proc. R. Soc. London, Ser. A* **2004**, *460*, 1849.
- [19] T. Castle, M. E. Evans, S. T. Hyde, S. Ramsden, V. Robins, *Interface Focus* **2012**, *2*, 555.
- [20] a) V. Robins, S. J. Ramsden, S. T. Hyde, *Eur. Phys. J. B* **2004**, *39*, 365; b) M. E. Evans, V. Robins, S. T. Hyde, *Acta Crystallogr., Sect. A: Found. Crystallogr.* **2013**, *69*, 241; c) S. Ramsden, V. Robins, S. Hyde, *Acta Crystallogr., Sect. A: Found. Crystallogr.* **2009**, *65*, 81.
- [21] M. O’Keeffe, M. A. Peskov, S. J. Ramsden, O. M. Yaghi, *Acc. Chem. Res.* **2008**, *41*, 1782.
- [22] W. Fischer, E. Koch, *Proc. R. Soc. London, Ser. A* **1996**, *354*, 2105.
- [23] a) P. J. Gandy, J. Klinowski, *Chem. Phys. Lett.* **2000**, *322*, 579; b) P. J. Gandy, J. Klinowski, *Chem. Phys. Lett.* **2000**, *321*, 363.
- [24] a) S. J. Callens, R. J. Uyttendaele, L. E. Fratila-Apachitei, A. A. Zadpoor, *Biomaterials* **2020**, *232*, 119739; b) C. M. Bidan, K. P. Kommareddy, M. Rumpfer, P. Kollmannsberger, Y. J. Brechet, P. Fratzl, J. W. Dunlop, *PLoS One* **2012**, *7*, e36336; c) L. Pieuchot, J. Marteau, A. Guignandon, T. Dos Santos, I. Brigaud, P.-F. Chauvy, T. Cloatre, A. Ponche, T. Petithory, P. Rougerie, M. Vassaux, J.-L. Milan, N. T. Wakhloo, A. Spangenberg, M. Bigerelle, K. Anselme, *Nat. Commun.* **2018**, *9*, 3995.
- [25] S. Truscello, G. Kerckhofs, S. Van Bael, G. Pyka, J. Schrooten, H. Van Oosterwyck, *Acta Biomater.* **2012**, *8*, 1648.
- [26] a) J. Tao, X. Song, B. Bao, S. Zhao, H. Liu, *Chem. Eng. Sci.* **2020**, *219*, 115602; b) F. Xu, M. Wei, X. Zhang, Y. Song, W. Zhou, Y. Wang, *Research* **2019**, *2019*, 2581241; c) K. Wang, Z. Chai, G. Hou, W. Chen, S. Xu, *Comput. Fluids* **2018**, *161*, 60.
- [27] Y. Jung, S. Torquato, *Phys. Rev. E* **2005**, *72*, 056319.
- [28] L. J. Gibson, M. F. Ashby, *Cellular Solids: Structure and Properties*, Cambridge University Press, **1999**.
- [29] V. Deshpande, M. Ashby, N. Fleck, *Acta Mater.* **2001**, *49*, 1035.
- [30] A. S. Dalaq, D. W. Abueidda, R. K. A. Al-Rub, *Composites, Part A* **2016**, *84*, 266.
- [31] S. Nachtrab, S. C. Kapfer, D. Rietzel, D. Drummer, M. Madadi, C. H. Arns, A. M. Kraynik, G. E. Schröder-Turk, K. Mecke, *Adv. Eng. Mater.* **2012**, *14*, 120.
- [32] O. Al-Ketan, A. Soliman, A. M. AlQubaisi, R. K. A. Al-Rub, *Adv. Eng. Mater.* **2018**, *20*, 1700549.
- [33] H. C. Tankasala, N. A. Fleck, *Int. J. Solids Struct.* **2020**, *188*, 233.
- [34] S. Janbaz, K. Narooei, T. van Manen, A. Zadpoor, *Sci. Adv.* **2020**, *6*, eaba0616.
- [35] a) M. Mansouri, H. Montazerian, S. Schmauder, J. Kadkhodapour, *Compos. Struct.* **2018**, *184*, 11; b) L. Wang, J. Lau, E. L. Thomas, M. C. Boyce, *Adv. Mater.* **2011**, *23*, 1524.
- [36] H. Montazerian, M. Mohamed, M. M. Montazeri, S. Kheiri, A. Milani, K. Kim, M. Hoorfar, *Acta Biomater.* **2019**, *96*, 149.
- [37] H. Montazerian, M. Zhianmanesh, E. Davoodi, A. Milani, M. Hoorfar, *Mater. Des.* **2017**, *122*, 146.
- [38] a) A. Fogden, S. Hyde, *Acta Crystallogr., Sect. A: Found. Crystallogr.* **1992**, *48*, 442; b) S. G. Markande, M. Saba, G. Schroeder-Turk, E. A. Matsumoto, *arXiv* **2018**.
- [39] J. U. Surjadi, L. Gao, H. Du, X. Li, X. Xiong, N. X. Fang, Y. Lu, *Adv. Eng. Mater.* **2019**, *21*, 1800864.
- [40] S. Kumar, S. Tan, L. Zheng, D. M. Kochmann, *npj Comput. Mater.* **2020**, *6*, 73.
- [41] C. Soyarslan, H. Argeso, S. Bargmann, *J. Mater. Res.* **2018**, *33*, 3371.
- [42] F. J. O’Brien, *Mater. Today* **2011**, *14*, 88.
- [43] K. J. Rambhia, P. X. Ma, *J. Controlled Release* **2015**, *219*, 119.
- [44] a) O. Al-Ketan, M. Pelanconi, A. Ortona, R. K. A. Al-Rub, *J. Am. Ceram. Soc.* **2019**, *102*, 6176; b) A. Rubio Carpio, F. Avallone, D. Ragni, M. Snellen, S. van der Zwaag, *Phys. Fluids* **2019**, *31*, 105110; c) W. Li, G. Yu, Z. Yu, *Appl. Therm. Eng.* **2020**, *179*, 115686; d) N. Sreedhar, N. Thomas, O. Al-Ketan, R. Rowshan, H. Hernandez, R. K. A. Al-Rub, H. A. Arafat, *Desalination* **2018**, *425*, 12.
- [45] a) J. Werner, G. Rodríguez-Calero, H. Abruña, U. Wiesner, *Energy Environ. Sci.* **2018**, *11*, 1261; b) C. Pouya, J. T. Overvelde, M. Kolle, J. Aizenberg, K. Bertoldi, J. C. Weaver, P. Vukusic, *Adv. Opt. Mater.* **2016**, *4*, 99; c) W. Yang, J. An, C. K. Chua, K. Zhou, *Virtual Phys. Prototyping* **2020**, *15*, 242.
- [46] E. Jin, I. S. Lee, D. Kim, H. Lee, W.-D. Jang, M. S. Lah, S. K. Min, W. Choe, *Sci. Adv.* **2019**, *5*, eaav4119.
- [47] M.-S. Pham, C. Liu, I. Todd, J. Lertthanasarn, *Nature* **2019**, *565*, 305.
- [48] K. M. Moerman, *J. Open Source Software* **2018**, *3*, 506.

- [49] W. Mickel, G. E. Schröder-Turk, K. Mecke, *Interface Focus* **2012**, 2, 623.
- [50] A. Fogden, S. T. Hyde, *Eur. Phys. J. B* **1999**, 7, 91.
- [51] N. S. Martys, J. G. Hagedorn, *Mater. Struct.* **2002**, 35, 650.
- [52] C. H. Arns, M. A. Knackstedt, W. V. Pinczewski, N. S. Martys, *J. Pet. Sci. Eng.* **2004**, 45, 41.
- [53] G. Dong, Y. Tang, Y. F. Zhao, *J. Eng. Mater. Technol.* **2019**, 141, 011005.
- [54] A. N. Gent, *Rubber Chem. Technol.* **1958**, 31, 896.